Advanced scanning electron microscopy techniques for structural characterization of zeolites

Natsuko Asano, Shunsuke Asahina, Jinfeng Lu, Jiani Xu, Yanfeng Shen, Zhengxing Qin, Svetlana Mintova

「Advanced scanning electron microscope techniques for the structural characterization of molecular sieves」

Natsuko ASANO[a], Shunsuke ASAHINA[a], Jinfeng LU[a], Jiani XU[b], Yanfeng Shen[b], Zhengxing QIN[b] and Svetlana MINTOVA[b,c]

[a]JEOL Ltd., 3-1-2 Musashino, Akishima, Tokyo, 196-8558, Japan

[b] State Key Laboratory of Heavy Oil Processing, College of Chemical Engineering, China University of Petroleum (East China), Qingdao, 266580, China

[c]Normandie Univ, ENSICAEN, UNICAEN, CNRS, Laboratoire Catalyse et Spectrochimie, 6 Boulevard Maréchal Juin, 14050 Caen, France.

Corresponding authors: Shunsuke ASAHINA and Zhengxing QIN

Abstract

In this work, low voltage high resolution FE-SEM observation and EDS analysis are used for the detailed investigation of zeolite structure. First, the advanced techniques and applications enabling the high-resolution imaging of crystal surface was demonstrated, and the operation parameters optimized, using a ZSM-5 zeolite with a mosaic surface morphology as the research model. Then, taking a SAPO-34 zeotype and its NH_4F treated counterpart as the demonstration models, high resolution surface and cross section imaging are combined to provide a comprehensive understanding of the porosity and inner architecture of the NH_4F etching derived hierarchical zeotype. The hidden macropores with a framed butterfly shape introduced by NH_4F etching is clearly revealed. In addition, the advantage of combined low voltage and triple-detectors EDS analysis in recording the near-surface-layer elements distribution is demonstrated. In the end, the possibility to follow the dissolution of SAPO-34 quasi in-situ by cross section imaging is shown for the first time. As a first observation, some inner parts of SAPO-34 are more vulnerable than the outermost shell of the crystals, which are preferentially removed in the beginning of NH_4F etching.

Introduction

Zeolites are a class of microporous materials with three-dimensional framework structure, consisting of TO_4 (T=Si, Al) tetrahedra linked by shared O atoms[1, 2]. Assembling of TO_4 units in zeolite frameworks results in the generation of regular cavities and channels, which are interconnected to form various micropore networks. Due to the micropores in the structures are unique and open to the outside allowing the mass transfer, zeolites are widely used in the ion exchange, adsorption and separation process[3-5]. Moreover, the active sites in the micropores allow the application of zeolites as a promising catalyst in chemistry industry[6]. However, although zeolites

are high porous, the micropore size is less than 2 nm even using extra-large pore type zeolites. The long diffusion distance and accumulation of the species in the micropores often lead to the pore-blockage and mass transfer limitation, causing the deactivation of zeolites[7, 8].

Many approaches have been designed to fabricate hierarchical structure in zeolites by introducing secondary meso-/macro-pores into the microporous framework, providing better access to micropores[9, 10]. In fabricating process, how to precisely characterize the inner architecture of zeolite plays an important role in understanding the hierarchical porosity system of zeolite crystals that determine their properties and potential applications. N_2 adsorption is a popular method for measuring the pore size distribution across the entire range of bulk zeolites[11]. By factoring the relative mesopore surface area and micropore volume, it is possible to calculate the porosity of hierarchical structure. However, it is hard to identify how the pores are distributed insight the zeolites from the bulk porous properties. In contrast, direct observing the location of mesopores and macropores in bulk zeolites using electron microscopy is notable to confirm the inner architecture of zeolites[12, 13]. And many imaging approaches have been developed to examine the pore architecture. Whereas, the micropores of zeolite are easily damaged by high-energy electrons, and the effect of charging electrons also make it difficult to obtain high-quality images[14]. Recently, with the development of electron microscope technology, low-voltage field emission scanning electron microscopy (FE-SEM) has been proven to be powerful for the imaging of electron-sensitive materials, such as the zeolites and mesoporous materials[15, 16]. When combining with cross section technology, the latest high-performance FE-SEM can provide new possibilities for us to investigate the inside of hierarchical structure zeolite particles. Moreover, the latest FE-SEM could significantly reduce the effect of charging phenomenon by selectively collecting high energy secondary electrons[17], as most of charging effect is caused by very low energy secondary electrons.

In addition, the spatial elements distribution analysis by an energy dispersive X-ray spectrometer (EDS) combined with FE-SEM also is an important approach for understanding the structure of zeolites. Because the introduction of secondary porosity into a microporous zeolite will cause partial removal of framework atoms, and the compositional change is very sensitive to the re-building of inner architecture[18]. Normally, acquiring a high-performance elements distribution map needs relatively long collecting time when using standard EDS. Furthermore, zeolite samples suffer from contamination and electron irradiation damage during the analysis process[19]. To improve the detection efficiency and precision, increasing the solid angle of EDS always is an essential issue in the development of EDS[20]. According to the definition of solid angle, producing a larger detection area using multi-detectors is effective to increase the solid angle, thus improving the detection efficiency of EDS even at low-voltage[21, 22].

In this study, Both ZSM-5 and SAPO-34 molecular sieves and their NH_4F treated counterparts were used as research models, with the goal to investigate the inner architecture of zeolite and zeolite

type materials by directly observing their structure change before and after NH_4F treatment through new developed FE-SEM. Moreover, by combining three EDS to FE-SEM, the element distribution of these two molecular sieves was featured.

Experimental

Materials

Preparation of parent and NH_4F treated ZSM-5 and SAPO-34

The synthesis of the parent ZSM-5 zeolite and its fluoride etching was carried out according to the recipes reported in our previous work[23]. The NH_4F treated ZSM-5 was prepared by NH_4F etching of the as-synthesized sample without calcination. The SAPO-34 molecular sieve was purchased from XFNANO company. The NH_4F treatment of parent SAPO-34 was carried out in 4 wt.% NH_4F solution. 2g SAPO-34 was added into 40g NH_4F solution and then the solution was stirred (400 rpm) at room temperature for 2.5 minutes. At last, the treated samples were collected by vacuum filtration, washed with deionized water and dried at 393 K. Their X-ray diffraction (XRD) patterns and N_2 sorption isotherm are presented in Figure S1. The treated sample remains the SAPO-34 crystal phase, however, with a decreased crystallinity (Figure S1a). This is in line with the loss in micropore sorption capacity (Figure S1b). On the other hand, the presence of mesoporosity is indicated by the presence of hysteresis loops in the N_2 physisorption-isotherms of the NH_4F treated SAPO-34 (Figure S1b).

Preparation of cross-section of SAPO-34 and its NH_4F etching

The cross-sections of SAPO-34 molecular sieve samples were prepared by using an Ar ion beam cross-section polisher (CP) with cooling system (IB-19530CP, JEOL). At first, the parent SAPO-34 and NH_4F treated SAPO-34 samples were embedded in the epoxy resin and then coated on a piece of Si wafer. After the resin hardened, the sample was set into the CP to produce a precise cross-section. Figure 1 shows a schematic of Ar ion beam milling. A shield plate was placed on top of the sample to determine its position. Only the portions uncovered by the shield plate were sputtered by Ar ion beam. The accelerating voltage of Ar ion beam was set as 4 kV and milling time was 4~12 hours. In addition, the sample holder was kept at -120 ℃ using liquid nitrogen. Since this liquid nitrogen cooling system could control the temperature of sample, proving much smoother and less-damage cross-sections. At last the cross-sections were coated with carbon using a carbon coater (thickness is 3 nm).

The NH_4F treatment of parent SAPO-34 cross-section without carbon coating was performed in 10 ml NH_4F solution (0.5 wt.%) at 293 K for 2.5 minutes. And then the cross-section was washed with deionized water and dried. Finally, this NH_4F treated cross-section was coated with carbon.

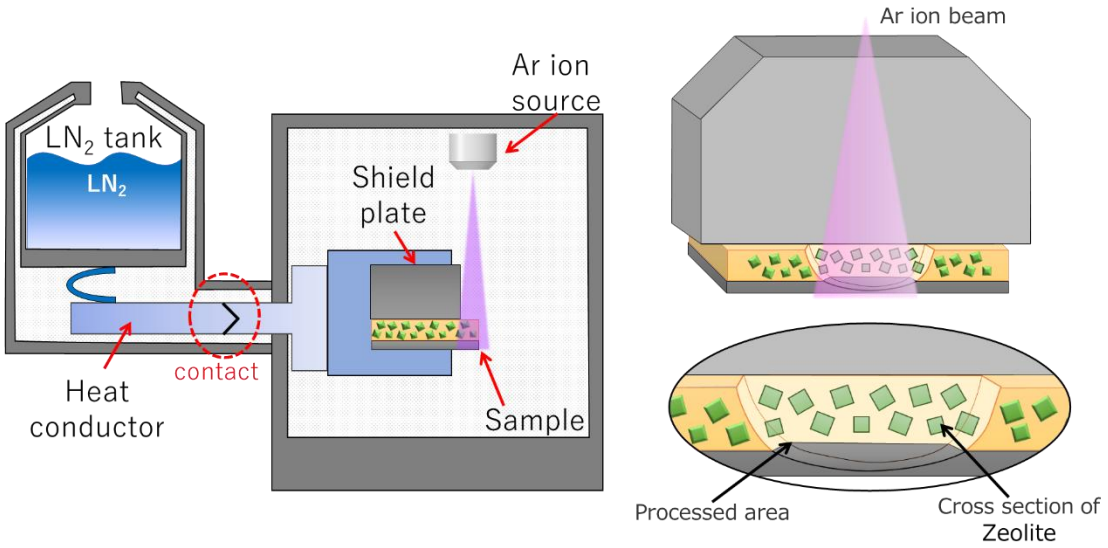

Figure 1. The cross sectioning using broad Ar ion beam.

Characterization

Direct observation of surface and cross section of molecular sieves was performed using FE-SEM (JSM-IT800SHL, JEOL). The observation conditions are discussed in the next section. The element distribution of SAPO-34 particles and its cross section was mapped by composing EDS detectors with FE-SEM. In this study, two EDS detectors (170 mm^2 sensor area, Ultim Max Oxford) and one windowless type EDS detector (100 mm^2 sensor area, Ultim Extreme Oxford) were used to obtain the element distribution maps. EDS analysis was performed at 3 kV, 5kV and 15 kV accelerating voltage, 700 pA probe current respectively. The acquiring time were 5 minutes. Because the zeolite samples are easily damaged by electron beam, all maps were obtained with one frame and one scan.

Results and discussion

Surface imaging

The surface imaging of zeolites and zeotypes by SEM is very sensitive to the primary electron beam. Varying the energy of primary electrons, different information can be obtained. Figure 2a illustrates a simulation result of interaction volume of incident electrons in the silicon using Monte Carlo simulation method. Notably, the incident electrons can diffuse into a depth of 200 nm from the surface and the diffusion width is larger than 200 nm when the accelerating voltage is set as 3 kV. However, although the high energy electrons can penetrate into the inner part of sample and emit a large number of electrons, the output of surface information is little, preventing the clear observation of surface structure. In contrast, the penetrated depth and width are less than 8 nm

when the accelerating voltage is reduced to 0.3 kV. In this case, the secondary electrons just generate from a narrow interaction area near the surface, which allows a clearer imaging of the nanostructure details on the sample surface. This can be seen clearly from the surface imaging of the parent ZSM-5 zeolite at different accelerating voltages (Figure 2b).

Moreover, applying a negative bias voltage to the zeolite samples can further reduce the effect of chromatic aberration caused by prime electron beam, improving the detection efficiency. Employing a new combined objective lens consisting of magnetic and electrostatic lenses (Figure 3a) to the observation could produce a small probe size, providing higher resolution. In addition, the choice of detector is also important in the observation of zeolites[24]. Various electrons emitted from the sample could be selectively detected by different detectors (Figure 3a), UED (upper electron detector) and UHD (upper hybrid detector). In this study, when we introduced these applications into the observation of ZSM-5 zeolite, high contrast images could be obtained (Figure 3b, 3c). According to the position of detector, as shown in Figure 3a, the UED could detect the low energy electrons which produces the edge contrast and the voltage contrast on the image (Figure 3b). While the UHD located in the objective lens could detect the high energy electrons which present the topography of samples without any effect of charge (Figure 3c). Moreover, applying a -5 kV bias voltage on the sample could make an accelerated beam decelerate just before landing on the sample surface, enabling a high-resolution observation. Finally, with these advanced and optimized technologies in hand, we are able to observe and compare confidently the subtle changes on zeolite surface. As an exemplify, Figure 4 shows the high-resolution SEM images of parent and NH_4F treated ZSM-5 zeolites. The crystallites of parent ZSM-5 exhibit an aggregated particle morphology with closely assembled nanoparticles on the surface (Figure 4a, 4b). After the etching by NH_4F, the shape of nanoparticles becomes smooth with little sharp corners and many mesopores appear between the nanoparticles as shown in Figure 4d. These results indicate that low-accelerating voltage is very appropriate for the high resolution surface observation.

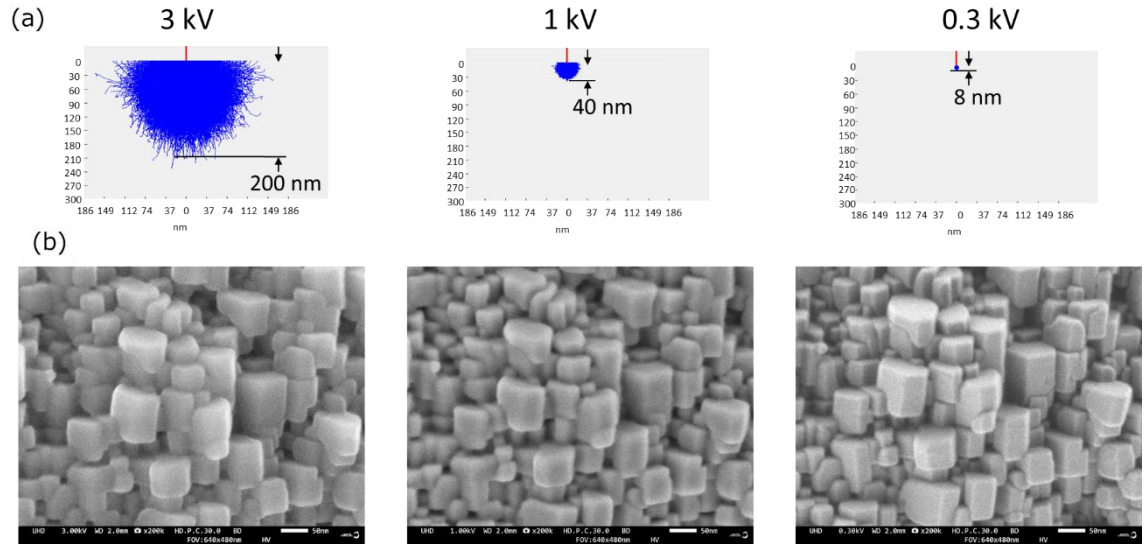

Figure 2. (a) Simulation result of interaction volume of incident electrons in the silicon using Monte Carlo simulation method (Calculated as SiO_2). (b) Comparison of SEM images of ZSM-5 obtained at different accelerating voltage: 3 kV, 1 kV, and 0.3 kV.

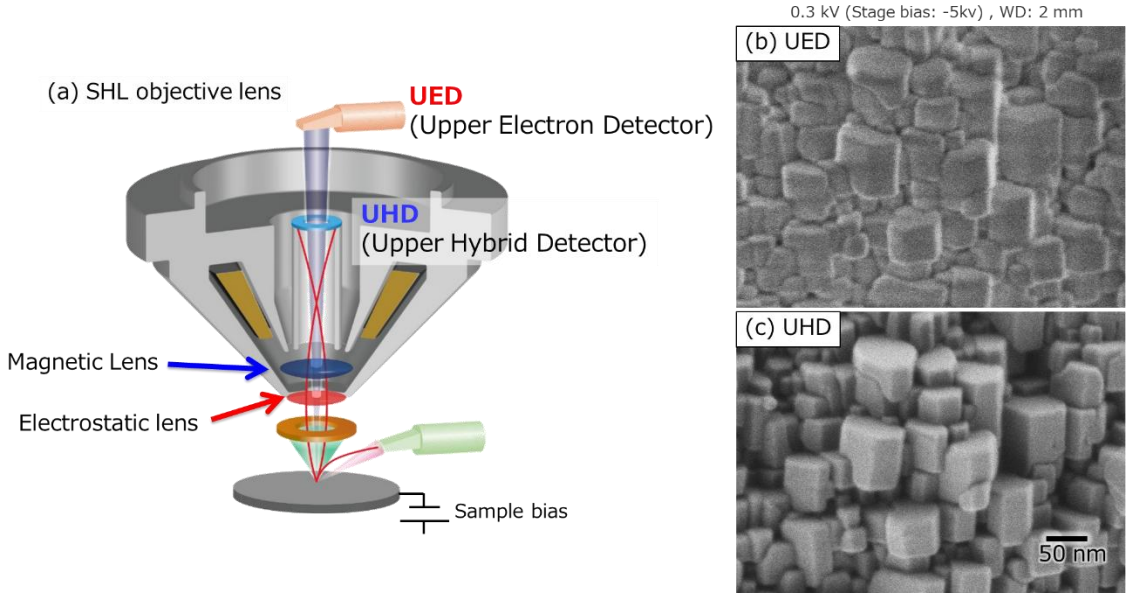

Figure 3. (a) The schematic drawing of objective lens and detection system of JSM-IT800SHL. (b) SEM image of ZSM-5 obtained with UED detector. (c) SEM image of ZSM-5 obtained with UHD detector

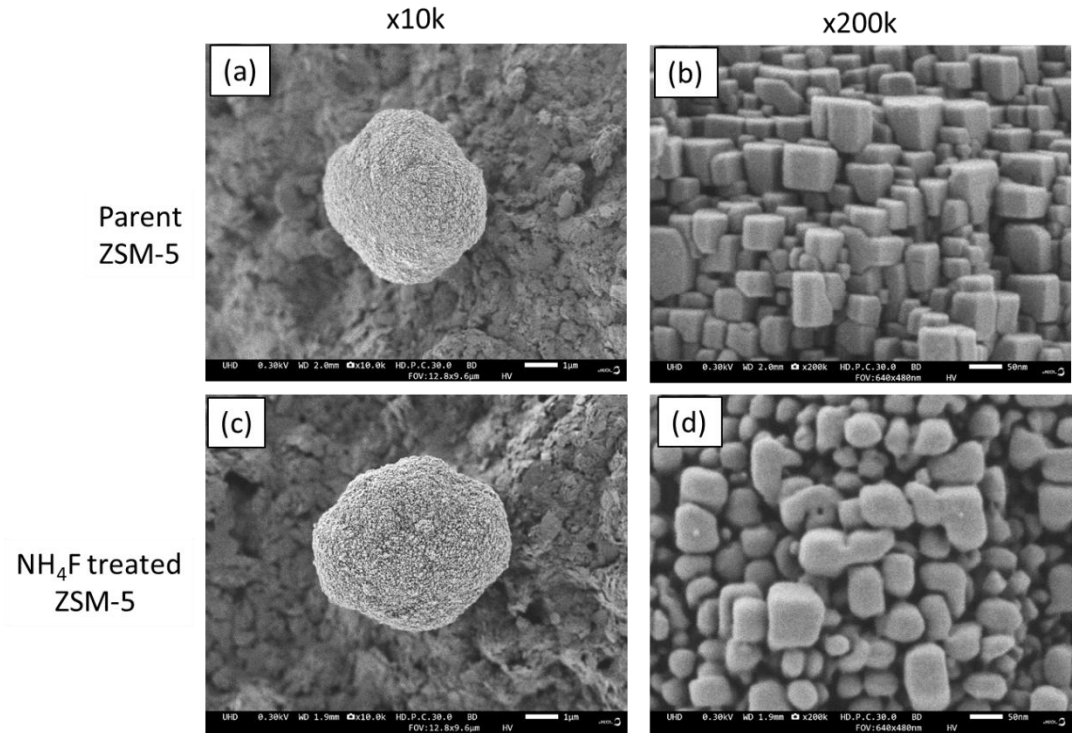

Figure 4. SEM images of (a) and (b) parent ZSM-5, (c) and (d) NH_4F-treated ZSM-5.

In the following, the low voltage observation is also applied to the surface imaging of SAPO-34, a zeotype material. Both the parent, purely microporous SAPO-34 and its NH_4F treated counterpart were inspected. The SEM image of the parent SAPO-34 particle exhibits that its shape is nearly cubic and the crystal size is much larger than 1 μ m, as shown in Figure 5a. The seemingly flat surface is essentially uneven, when increasing the observing magnification from 10K to 200K under low voltage condition (Figure 5b). This should be associated with the surface growth during the final stage of crystallization, which reflects the dynamic equilibrium between dissolution and nucleation. Figure 5c shows the morphology of the NH_4F treated SAPO-34. The high-resolution imaging of the remarkably roughened surface presents a dense distribution of mesopores (Figure 5d). With this and the N_2 physisorption information (Figure S1b) in mind, one may speculate that this is a highly mesoporous sample.

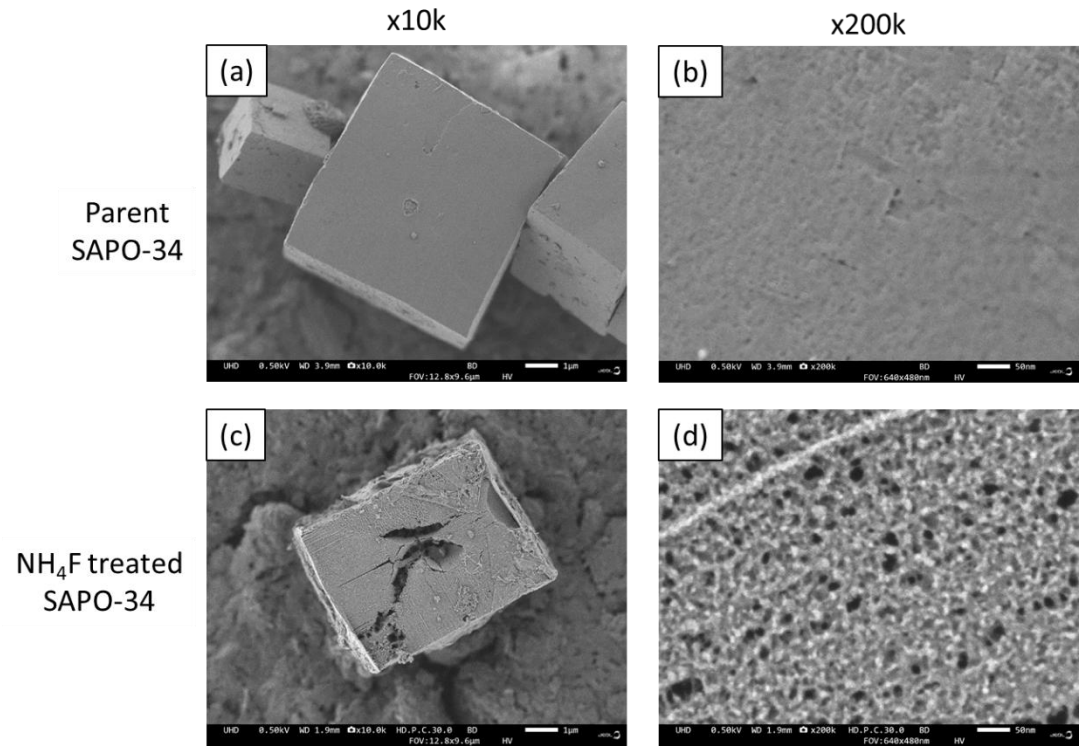

Figure 5. The morphology of the parent and NH_4F treated SAPO-34 samples. (a) SEM image of parent particle, (b) Surface of (a), (c) SEM image of NH_4F treated particle, (d) Surface of (c)

Cross section imaging and the comparison with surface imaging

Besides the high-resolution imaging of sample surface showing the presence of mesoporosity, many other information including mesopore morphology, connectivity and spatial distribution are also very important and may guide the optimization and applications of zeolites and zeotype materials. Here we show the convenience, intuitive visibility and comprehensiveness of the cross section imaging in characterization of the mesoporosity beneath the outer surface of mesoporous materials. Microporous SAPO-34 and its NH_4F treated counterpart were used as the research models. The samples were cut with an ion beam cross sections polisher (CP) and SEM images are displayed in Figure 6. Compared to the irregular interface exposed by crashing sample with mortar, the CP cross sections are flat surfaces without any deposition (Later it will be shown that a flat surface is favorable for the precise analysis of elements distribution). The cross section image of the parent SAPO-34 expresses a specific internal structure without obvious pores or other defects. In contrast, NH_4F etching results in a framed pattern of butterfly-shape (Figure 6c). Between the frame and the butterfly-shape there are many macroporous holes, suggesting that the inner part of SAPO-34 crystals is preferentially dissolved, while the outermost shell is resistant. The inhomogeneous dissolution has reached up to 0.5-1.0 μ m in the particles and the thickness of the remaining shell

is less than 50 nm. This porosity information is quite different from the one interpreted from the imaging of the outermost shell in many aspects, such as the pore size, morphology, density, and the uniformity of spatial distribution. In particular, when magnifying the images of surface and cross section to compare the "mesoporosity" from different perspective in detail (Figure 7), the high mesoporosity of NH_4F treated SAPO-34 interpreted from Figure 5d seems to be far from representative. Namely, the dense mesopores area (Region A) actually represent only a thin layer on the surface. Nevertheless, the comparison of the surface and cross section images allows a more comprehensive understanding of the secondary porosity in the NH_4F treated SAPO-34. The macro defects area (Regions B) corresponds to some cracks on the shell of cross section with different sizes, the nanofibers formed at the surface (Region C) are clearly confirmed on the thick shell of cross section, to name a few.

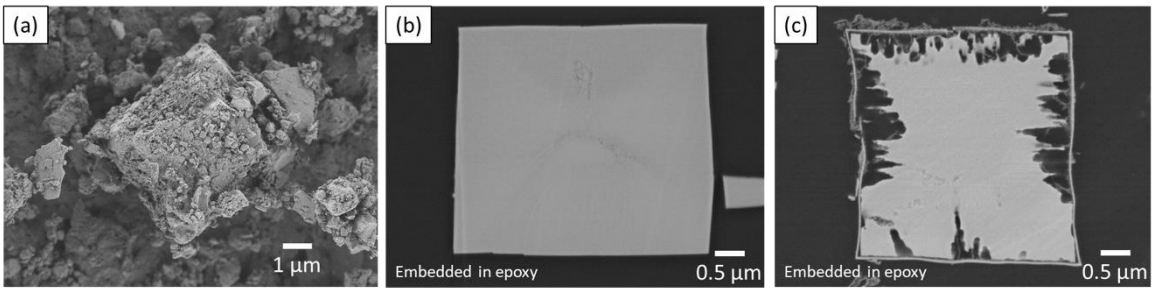

Figure 6. SEM images of cross section of the parent and NH_4F treated SAPO-34 samples. (a) Mortar crashed parent sample (b) CP cross section of parent particle (c) CP cross section of NH4F treated particle.

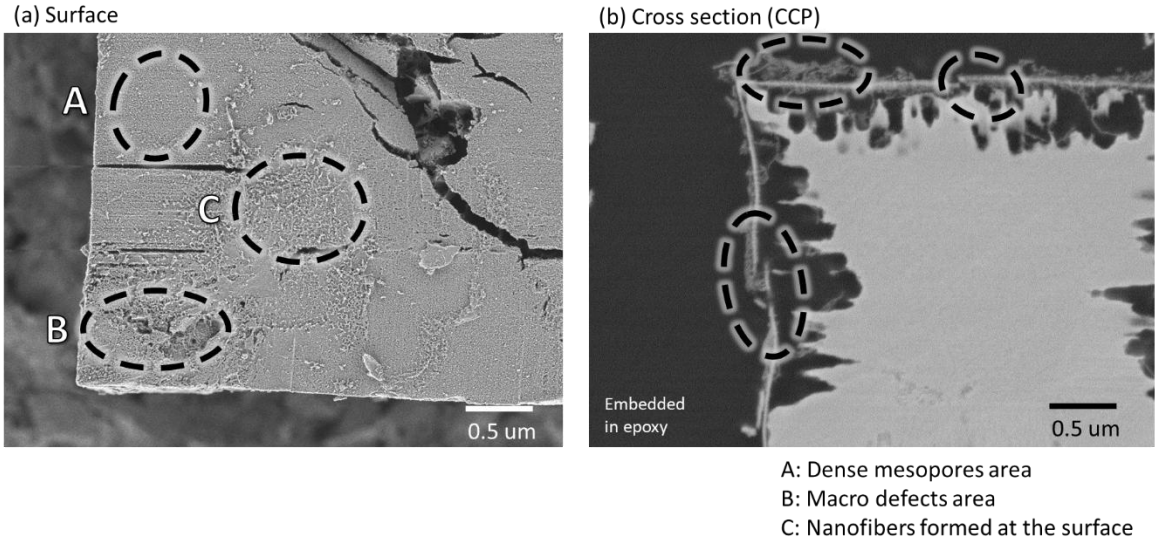

Figure 7. Comparison of magnifying images of (a) particle surface and (b) cross section of NH_4F treated SAPO-34 samples. A, B, C in Figure 7a and b show dense mesopores area, macro defects area and nanofibers formed at the surface, respectively.

Low voltage and triple-detectors EDS analysis

Besides the comprehensive observation of the secondary porosity from different perspectives (Figure 7), a precise documentation of the distribution of different elements at a single crystal level is also important, as it can be very helpful for the interpretation of crystallization mechanism[23] and catalytic behavior[6, 7]. Here we show the advantage (high spatial resolution, available near-surface-layer information, etc) of combined low voltage and triple-detectors EDS analysis in recording the near-surface-layer elements distribution in SAPO-34 crystals. The cross-sections of the parent and treated SAPO-34 particles were used as the specimens, as these samples prepared by CP is flat (Figure 6b, c), there is no shadow of samples in the EDS maps, which is favorable for determining surface layer elements distribution. Moreover, the information extracted from the cross-section is very helpful for the interpretation of the spatial elements distribution in the inner part of zeolite crystals[23].

For EDS analysis, there are two important factors in determining the performance. Namely, SEM condition affects the spatial resolution of EDS analysis and the solid angle of detector affects the collection number of characteristic X-rays. The previous reports have confirmed that low accelerating voltage, namely low incident electrons energy, is suitable for the surface observation, which is also effective for the surface analysis by EDS[25]. In Figure 8, the generation volume of characteristic X-rays was simulated under different incident electrons energy. When we set the accelerating voltage as 15 kV, a normal high energy condition for EDS analysis, the penetration depth of incident electrons in the sample has reached to 3 μm and the diffusion width is also very large, causing a large generation volume of characteristic X-rays. A large number of characteristic X-rays generated from the inner part of sample were collected as the information of analyzing point, which reduce the spatial resolution of EDS mapping significantly. While reducing the accelerating voltage to 3 kV, the penetration of incident electrons stops near the sample surface and the incident electrons just diffuse in a narrow area, providing a high spatial resolution.

For compassion, the elements distribution in the cross-section of the parent and treated SAPO-34 particles was mapped using EDS at both 15 kV and 3 kV. A detector set at the back of chamber was used to obtain the maps shown in Figure 9. In good agreement with the simulation result in Figure 8, while the large generation volume of X-rays enlarges the distribution area of elements in 15 kV EDS analysis (Figure 9a), characteristic X-rays only generated from the near surface of particles when using low voltage 3 kV. The edge contrast of maps obtained at 3 kV is obviously sharp (Figure 9b) due to the little information from the inside of cross section. Even the mapping images have less sharpness, a stronger Si and O detection with the very weak signal of element Al also can be detected from the shell when using 3 kV.

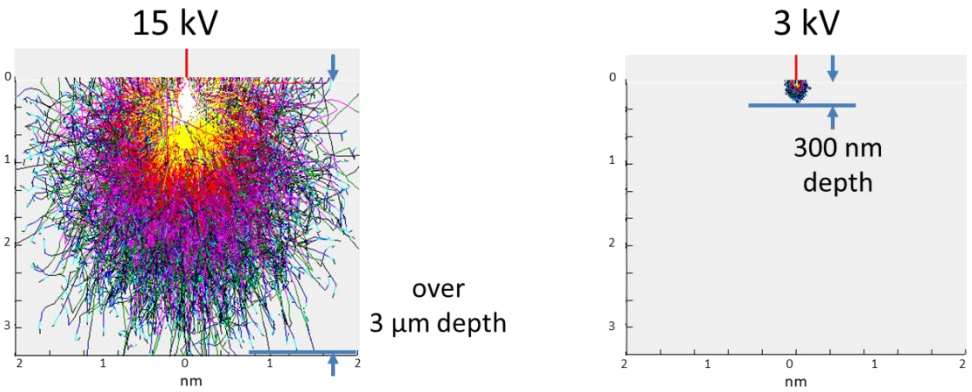

Figure 8. Simulation result of characteristic X-rays generation volume in the silicon using Monte Carlo simulation method.

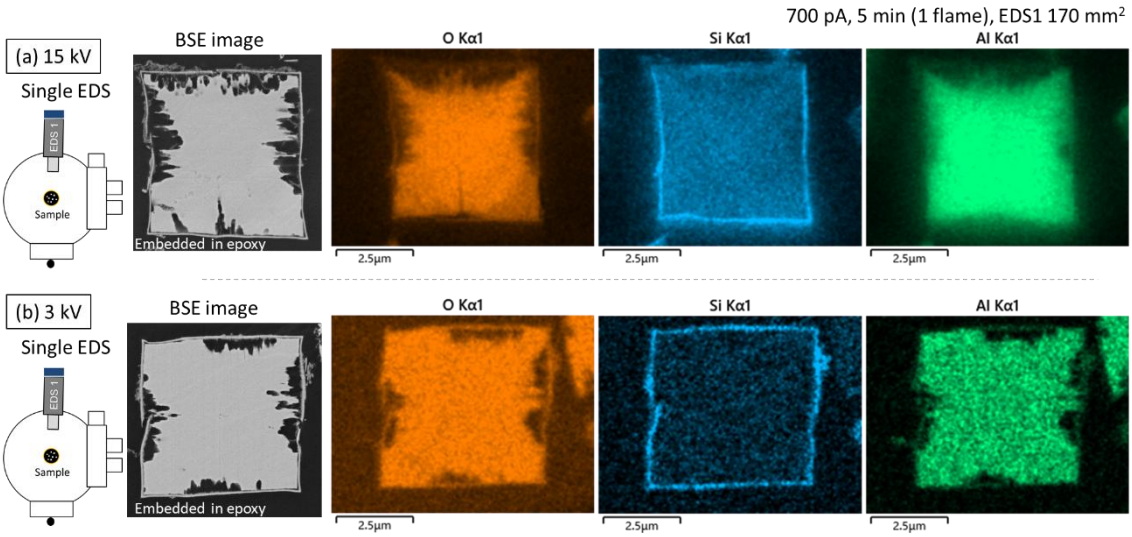

Figure 9. Element distribution maps of parent and NH_4F treated SAPO-34 obtained using one EDS detector.

Although a decrease of the accelerating voltage is favorable for surface analysis, reducing incident electrons energy also implies that less X-rays are generated. How to maximize the collection efficiency of characteristic X-rays plays an essential role in determining the quality of EDS analysis when using low accelerating voltage. An important factor to define the sensitivity of detector is the solid angle of EDS detector. The solid angle is a three-dimensional angle formed by the cross-sectional detection area (sphere) of the detector with respect to the analysis point. Only those characteristic X-rays in the hemisphere area limited by solid angle of detector are eligible for detection. A large solid angle enables a larger detecting number of characteristic X-rays.

The solid angle can be made larger for a larger sensor area and a smaller distance between the

sample and the detector. In order to enhance the detection efficient and reduce the effect of noise, in this study, EDS maps for Si, Al, P and O were collected from parent SAPO-34 and its cross sections with two EDS detectors (170 mm^2 sensor area, Ultim Max Oxford) and one windowless type EDS detector (100 mm^2 sensor area, Ultim Extreme Oxford). These three EDS detectors were used simultaneously to obtain the element maps. To achieve the best sensitivity, the detectors were inset to a position as close as possible to the sample (Figure 10). Consequently, the solid angle become very large by amounting the sensor area of three detectors. In addition, three detectors were settled in the chamber from different direction, which can provide high quality EDS maps without any shadow even for the bulk sample. As shown in the schematic drawing (Figure 10a), the significant improvement of detection area enables a very high solid angle of EDS detecting, providing high detection efficient for EDS analysis. Therefore, the maps with little noise can be acquired even using low voltage 3 kV. The element maps and line scans exhibit a clear Si-rich shell and an Al-rich inner crystal in the parent and NH_4F treated SAPO-34.

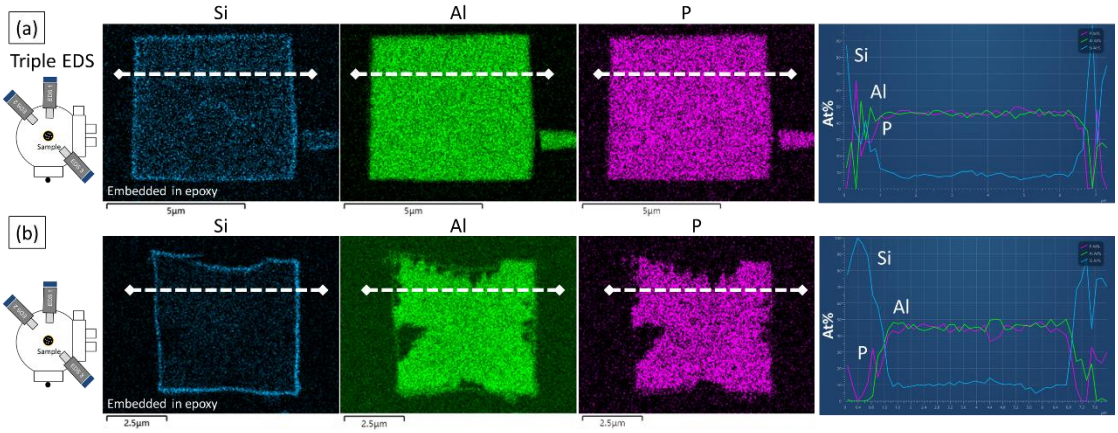

Figure 10. Element distribution maps and line profiles of (a) Parent and (b) NH4F treated SAPO-34 obtained using three EDS detectors.

Quasi in-situ observing the NH_4F etching of SAPO-34 by cross section imaging

Seeing is believing. A vivid tracking of crystal dissolution behavior in-situ could be very interesting. Previously, the time resolved changes in surface topography during the NH_4F etching of MFI-type zeolite crystals was examined by atomic force microscopy[26]. In the present work, we show for the first time the possibility to follow the dissolution of SAPO-34 quasi in-situ by cross section imaging. For this purpose, the low vacuum backscattered electron detector (LV-BED) was used for imaging. The observation performed at low-vacuum also can reduce the effect of charge electrons through introducing N_2 gas into the chamber, while keeping the column of SEM at high vacuum through an orifice control. Because N_2 gas irradiated by electron beam could be ionized and then reacts with charge electrons, a clear image without charge effect can be obtained by the LV-BED attached on

the orifice control.

To investigate the effect of NH_4F etching in the particle, the cross section of parent SAPO-34 (Figure 11a) was treated by NH_4F directly. The backscattered electron images of cross section before and after etching was recorded immediately after the sample preparation (Figure 11a and 11b). The compassion of the images shows unambiguously that the treated cross section exhibits an obvious spatially inhomogeneous etching (Figure 11b). Combining with the EDS analysis result (Figure 11c), the outmost and Si-rich shell (Figure 10) is remained, while the etching starts from the parts below the shell. This is the first record that shows the initial dissolution sites during the NH_4F etching of SAPOs. Also, this is the first evidence showing that some inner part of SAPO-34 is more vulnerable than the outermost shell of the crystals. As a result, the inner parts are preferentially removed during NH_4F etching. The dissolution front should point to the center of the crystal. Besides, the dissolution should start parallelly from the 6 faces of SAPO-34 crystals. This accounts for the formation of the porous structure with the characteristic 2-dimentional butterfly morphology (Figures 6-7 and Figures 9-10). One can imagine that with a further extension of the chemical etching, the butterfly-shaped domains will continuous shrinkage until the central part disappears [Add references here: Hollow SAPO-34 Cubes with Hierarchically Organized Internal Structure; Creation of hollow SAPO-34 single crystals via alkaline or acid etching; In situ growth-etching approach to the preparation of hierarchically macroporous zeolites with high MTO catalytic activity and selectivity].

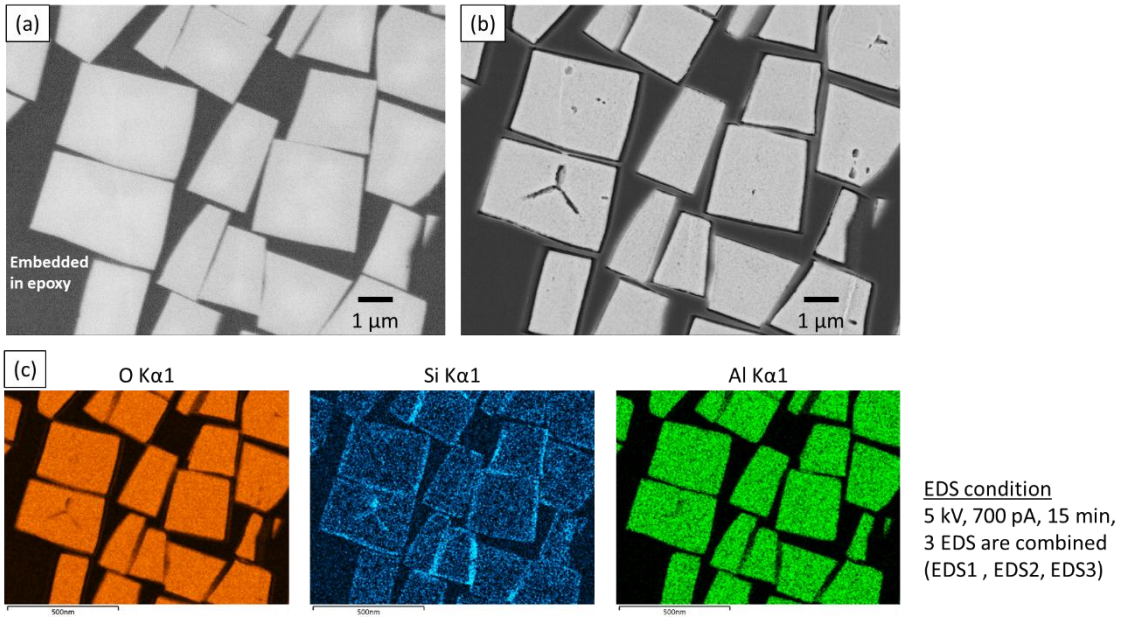

Figure 11. SEM images and element maps of the cross section of SAPO-34 before and after NH_4F treatment. (a) SEM image of cross section before treatment. (b) SEM image of cross section after treatment. (c) Element distribution maps of (b). EDS conditions: 5kV, 700 pA, 15 min, 3 EDS (EDS1,

EDS2 and EDS3, Figure 10) are combined.

Conclusions

In this work, the inner architecture and crystal surface of a SAPO-34 zeotype and its NH_4F treated counterpart were investigated using a low voltage FE-SEM. Thanks to the low penetration depth and small damage on the zeolite, low voltage FE-SEM is favorable for the high resolution observation and analysis of zeolite structure. The high-resolution SEM images of the NH_4F treated zeotype represent a surface consisting of dense mesopores and macro defect areas. However, the cross sections of the treated sample prepared by an Ar ion polisher indicate a butterfly-shaped porous pattern with a Si-rich shell and an Al-rich inner part in the particle. These results suggest a spatially inhomogeneous etching of framework and serve as a more comprehensive understanding of the hierarchical structure, which specify the spatial morphology and location of the derived mesopores and macro cavities. In addition, cross section imaging with low voltage and high-resolution FE-SEM was used for the first time quasi in-situ to document the initial dissolution point during the NH_4F etching of SAPO-34. it is revealed that the etching reaction starts from the inner part of crystals and then diffuse rapidly towards crystal center to form a porous structure with a butterfly pattern.

Conflicts of interest

There are no conflicts to declare.

Acknowledgements

Z.Q. acknowledges the support from NSFC 22178389; S.M acknowledges the support from NSFC 21975285, NSFC 22175200; Z.Q. and S.M. acknowledge the support from NSFC 21991090, NSFC21991091.

Supporting information

Notes and references

1. J. M. Newsam, The zeolite cage structure, *Science*, 1986, **231** (4742), 1093-1099.
2. L.Tosheva and V. Valtchev, Nanozeolites: Synthesis, Crystallization Mechanism, and Applications, *Chem. Mater*., 2005, **17**, 2494−2513.
3. C. Colella, Ion exchange equilibria in zeolite minerals, *Miner. Depos.*, 1996, **31**, 554-562.
4. P. Li and F. H. Tezel, Adsorption separation of N_2, O_2, CO_2 and CH_4 gases by β-zeolite, *Micro. Meso. Mater.*, 2007, **98** (1-3), 94-101.
5. H. Liu, D. Yuan, L. Yang, J. Xing, S. Zeng, S. Xu, Y. Xu and Z. Liu, Directly decorated CeY zeolite for O_2-selective adsorption in O_2/N_2 separation at ambient temperature, *Mater. Horiz.*, 2022, **9**,

688-693.

6. B.M. Weckhuysen and J. Yu, Recent advances in zeolite chemistry and catalysis, *Chem. Soc. Rev.*, 2015, **44** (20), 7022-7024.
7. G. Elordi, M. Olazar, G. Lopez, P. Castano and J.Bilbao, Role of pore structure on the deactivation of zeolite (HZSM-5, Hβand HY) by coke in the pyrolysis of polyethylene in a conical spouted bed reactor, *Appl. Catal. B*, 2011, **102** (1-2), 224-231.
8. F. C. Hendriks, D. Valencia, P. C. A. Bruijnincx and B. M. Weckhuyen, Zeolite molecular accessibility and host-guest interactions studied by adsorption of organic probes of tunable size, *Phy. Chem. Chem. Phys.*, 2017, **19**, 1857-1867.
9. L. Chen, M. Sun, Z. Wang, W. Yang, Z. Xie and B. Su, Hierarchically structured zeolites: from design to application, Chem. Rev., 2020, **120** (20), 11194-11294.
10. G. Yang, J. Han, Y. Huang, X. Chen and V. Valtchev, Busting the efficiency of SAPO-34 catalysts for the MTO conversion by post-synthesis methods, Chin. J. Chem. Eng., 2020, **28**(8), 2022-2027.
11. A. Galarneau, F. Villemot, J. Rodriguez, F. Fajula, and B. Coasne, Validity of the *t*-plot method to assess microporosity in hierarchical micro/mesoporous materials, *Langmuir*, 2014, **30**, 13266-13274.
12. L. I. Meza, M. W. Anderson, B. Slater and J. R. Agger, In situ atomic force microscopy of zeolite A dissolution, *Phy. Chem. Chem. Phy.*, 2008, **10**, 5066-5076.
13. W. wan, J. Su, X. Zou and T. Willhammar, Transmission electron microscopy as an important tool for characterization of zeolite structures, *Inorg. Chem. Front.*, 2018, **5**, 2836-2855.
14. R. Csencsits and R. Gronsky, Damage of zeolite Y in the TEM and its effects on TEM images, *Ultramicroscopy*, 1987, **23** (3-4), 421-431.
15. X. Zhang, X. Cen, R. Ravichandran, L. A. Hughes, and K. v. Benthem, Simultaneous scanning electron microscope imaging of topographical and chemical contrast using In-lens, In-column, and Everhart-Thornley detector systems, *Microsc. Microanal.*, 2016, **22** (3) 565-575.
16. S. Che, K. Lund, T. Tatsumi, S. Iijima, S. H. Joo, R. Ryoo and O. Terasaki, Direct observation of 3D mesoporous structure by scanning electron microscopy (SEM): SBA-15 silica and CMK-5 carbon, *Angew. Chem.*, 2003, **42**(19), 2182-2185.
17. M. Suga, S. Asahina, Y. Sakuda, H. Kazumori, H. Nishiyama, T. Nokuo, V. Alfredsson, T. Kjellman, S. M. Stevens, H. S. Cho, M. Cho, L. Han, S. Che, M. W. Anderson, F. Schuth, H. Deng, O. M. Yaghi, Z. Liu, H. Y. Jeong, A. Stein, K. Sakamoto, R. Ryoo and O. Terasaki, Recent progress in scanning electron microscopy for the characterization of fine structural details of nano materials, *Prog. Solid. State Ch.*, 2014, **42**, 1-21.
18. Y. Wang, M. Lin and A. Tuel, Hollow TS-1 crystals formed via a dissolution–recrystallization process, *Microporous Mesoporous Mater.*, 2007, **102**(1), 80–85.

19. J. J. Friel and C. E. Lyman, X-ray mapping in electron-beam instruments, *Microsc. Microanal.*, 2006, **12**, 2-25.
20. N. J. Zaluzec, Detector solid angle formulas for use in X-rays energy dispersive spectrometry, *Microsc. Microanal.*, 2009, **15**(2), 93-98.
21. M. Procop, V. hodoroaba, R. Terborg, D. Berger, Determination of the effective detector area of an energy-dispersive X-ray spectrometer at the scanning electron microscope using experimental and theoretical X-ray emission yields, *Microsc. Microanal.*, 2016, **22**(6), 1-9.
22. S. Koshiya and K. Kimoto, Improvement of effective solid angle using virtual-pivot holder and large EDS detector, *Micro.*, 2017, **93**, 52-56.
23. Y. Shen, Z. Qin, S. Asahina, N. Asano, G. Zhang, S. Qian, Y. Ma, Z. Yan, X. Liu and S. Mintova, The inner heterogeneity of ZSM-5 zeolite crystals, *J. Mater. Chem. A*, 2021, **9**, 4203-4212.
24. S. Asahina, T. Togashi, O. Terasaki, S. Takami, T. Adschiri, M. Shibata and N. Erdman, High-resolution low voltage scanning electron microscope study of nanostructured materials, *Microsc. Microanal.*, 2012, **26** (7), S12-S14.
25. N. Asano, J. Lu, S. Asahina and S. Takami, Direct observation techniques using scanning electron microscope for hydrothermally synthesized nanocrystals and nanoclusters, *nanomaterials*, 2021, **11**, 908.
26. K. N. Bozhilov, T. Thanhle, Z. Qin, A Palčić, J. D. Rimer and V. Valtchev, Time-resolved dissolution elucidates the mechanism of zeolite MFI crystallization, Sci. Adv., 2021, 7 (25), 1-10.

Figure caption

Figure 1. The cross sectioning using broad Ar ion beam.

Figure 2. (a) Simulation result of interaction volume of incident electrons in the silicon using Monte Carlo simulation method. (b) Comparison of SEM images of ZSM-5 obtained at different accelerating voltage 3 kV and 0.3 kV.

Figure 3. (a) The schematic drawing of objective lens and detection system in a scanning electron microscope. (b) SEM image of ZSM-5 obtained with UED detector. (c) SEM image of ZSM-5 obtained with UHD detector

Figure 4. Simulation result of characteristic X-rays generation volume in the silicon using Monte Carlo simulation method.

Figure 5. SEM images of parent ZSM-5 and post-treated ZSM-5 by NH_4F.

Figure 6. The morphology of the parent and NH_4F treated SAPO-34 samples. (a) SEM image of parent particle (b) Surface of (a) (c) SEM image of NH_4F treated particle (d) Surface of (c)

Figure 7. SEM images of cross section of the parent and NH_4F treated SAPO-34 samples. (a) Mortar crashed parent sample (b) CP cross section of parent particle (c) CP cross section of NH4F treated particle.

Figure 8. Comparison of magnifying images of particle surface and cross section of NH_4F treated SAPO-34 samples

Figure 9. Element distribution maps of parent and NH_4F treated SAPO-34 obtained using one EDS detector.

Figure 10. Element distribution maps of parent and NH4F treated SAPO-34 obtained using three EDS detectors. (a) Schematic drawing of three EDS detectors (b) Element maps

Figure 11. SEM images and element maps of the cross section of SAPO-34 before and after NH_4F treatment. (a) SEM image of cross section before treatment (b) SEM image of cross section after treatment (c) Element maps of cross section before treatment (d) Element maps of cross section after treatment.